Seafloor Observations Eliminate a Landslide as the Source of the 1918 Puerto Rico Tsunami

Uri ten Brink[*1], Jason Chaytor[1], Claudia Flores[1], Yong Wei[2,3], Simon Detmer[4], Lilian Lucas[5], Brian Andrews[1], and Aggeliki Georgiopoulou[6,7]

ABSTRACT

The 11 October 1918 devastating tsunami in northwest Puerto Rico had been used as an example for earthquake-induced landslide tsunami hazard. Three pieces of evidence pointed to a landslide as the origin of the tsunami: the discovery of a large submarine landslide scar from bathymetry data collected by shipboard high-resolution multibeam sonar, reported breaks of submarine cable within the scar, and the fit of tsunami models to flooding observations. Newly processed seafloor imagery collected by remotely operated vehicle (ROV) show, however, pervasive Fe–Mn crust (patina) on the landslide walls and floor, indicating that the landslide scar is at least several hundred years old. ^{14}C dates of sediment covering the landslide floor verify this interpretation. Although we have not searched the region systematically for an alternative tsunami source, we propose a possible source—a two-segment normal-fault rupture along the eastern wall of Mona rift. The proposed fault location matches the published normal faults with steep bathymetry and is close to the International Seismological Center–Global Earthquake Model catalog locations of the 1918 mainshock and aftershocks. The ROV observations further show fresh vertical slickensides and rock exposure along the proposed fault trace. Hydrodynamic models from an M_w 7.2 earthquake rupture along the eastern wall of the rift faithfully reproduce the reported tsunami amplitudes, polarities, and arrival times. Our analysis emphasizes the value of close-up observations and physical samples to augment remote sensing data in natural hazard studies.

KEY POINTS

- Seafloor observations indicate that a landslide could not be the source of the 1918 Puerto Rico tsunami.
- Tsunami from an M_w 7.2 rupture of a two-segment fault in eastern Mona rift fits the observations well.
- Our analysis shows the need for seafloor observations and sampling in natural hazard studies.

INTRODUCTION

The damaging 11 October 1918 earthquake offshore northwest Puerto Rico was followed within minutes by a tsunami that mostly affected the west coast of Puerto Rico. The tsunami caused more than 100 casualties, and the damage exceeded $4,000,000 in 1918 U.S. dollars (Reid and Taber, 1919). A repeat of such an event today has the potential to be catastrophic due to the increased population, tourism, and development along the coast of Puerto Rico. Hence, the interest in understanding the source of the event. The location and focal mechanism of the earthquake and aftershocks could not be determined with certainty, given the small number of operating seismometers globally and the lack of any local instruments at the time (Location quality of B and C in the International Seismological Center–Global Earthquake Model (ISC-GEMS) catalog (Di Giacomo *et al.*, 2018). The most recent estimate by ISC-GEMS, also adopted by the U.S. Geological Survey (USGS) Advanced National Seismic Systems Comprehensive Catalog, is several kilometers east of the eastern boundary of Mona rift (Fig. 1) (18°42′ –67°11.34′) with aftershocks of estimated magnitudes between M_w 5.8 and 6.35, located along the eastern boundary of the rift (ISC-GEMS catalog). An earlier epicentral estimate (Russo and Bareford,

1. U.S. Geological Survey, Woods Hole, Massachusetts, U.S.A., https://orcid.org/0000-0001-6858-3001 (UtB); https://orcid.org/0000-0003-0676-7061 (CF); https://orcid.org/0000-0003-1024-9400 (BA); 2. Cooperative Institute for Climate, Ocean, and Ecosystem Studies, University of Washington, Washington, U.S.A., https://orcid.org/0000-0002-6908-1342 (YW); 3. NOAA-PMEL, Seattle, Washington, U.S.A.; 4. Department of Geology, Geography, and Environment, Calvin University, Grand Rapids, Michigan, U.S.A., https://orcid.org/0000-0003-3726-6825 (SD); 5. Department of Geology, University of Illinois at Urbana-Champaign, Urbana, Illinois, U.S.A., https://orcid.org/0000-0001-5344-6012 (LL); 6. UCD School of Earth Sciences, University College Dublin, Belfield, Ireland, https://orcid.org/0000-0003-4298-5090 (AG); 7. Now at Ternan Energy, Chichester, United Kingdom

*Corresponding author: utenbrink@usgs.gov

Cite this article as ten Brink, U., J. Chaytor, C. Flores, Y. Wei, S. Detmer, L. Lucas, B. Andrews, and A. Georgiopoulou (2023). Seafloor Observations Eliminate a Landslide as the Source of the 1918 Puerto Rico Tsunami, *Bull. Seismol. Soc. Am.* **113**, 268–280, doi: 10.1785/0120220146

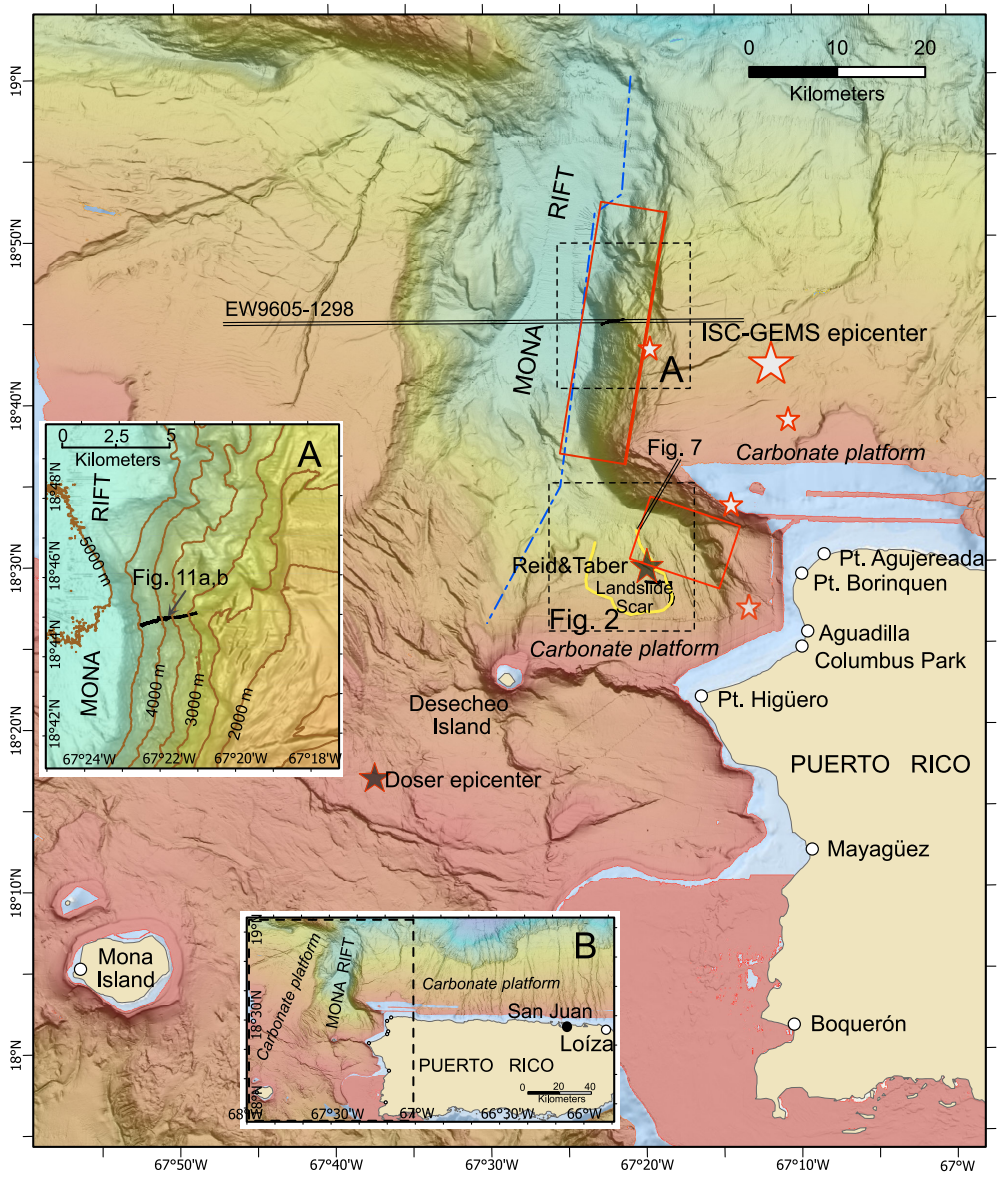

Figure 1. Shaded relief bathymetry of Mona rift and Mona Passage off western Puerto Rico. Circles denote reported observations sites of tsunami flooding listed in Table 2. Solid red rectangles denote surface projection of the two-segmented normal fault, modeled as the tsunami source (see the Discussion—segmented fault as tsunami source section). Dashed–dotted blue line denotes tsunami source fault modeled by Mercado and McCann (1998). Yellow curve denotes landslide tsunami source of López-Venegas *et al.* (2008, 2015). Large and small white stars denote proposed epicenter of the 1918 earthquake and aftershocks (International Seismological Center–Global Earthquake Model [ISC-GEMS] catalog). Black stars denote proposed epicenter of Doser *et al.* (2005) and isoseismal epicenter of Reid and Taber (1919). Black lines denote remotely operated vehicle (ROV) dive tracks NA035-H1301 and EX-1502-05. Double lines denote seismic lines Pelican Line 62 shown in figure 7 and EW9605-1298 shown in figure 8 of Mondziel *et al.* (2010). Dashed rectangle denotes location of inset A. Inset A shows the enlargement of the eastern wall of Mona rift with dive track EX-1502-05. Brown contours denote 500 m depth contours. Inset B shows the regional location map showing extent of map (dashed rectangle) and location of the Loíza site in Puerto Rico. The color version of this figure is available only in the electronic edition.

1993), quoted by Doser *et al.* (2005), was located within Mona Passage (18°16.8′ −67°37.2′, Fig. 1) with an estimated location uncertainty of 50 km. However, seismic and multibeam bathymetry data do not show a recent seafloor or subseafloor rupture in the vicinity of the Doser *et al.* (2005) epicenter (Chaytor and ten Brink, 2010). The proposed magnitude of the mainshock is M_w 7.1 ± 0.3 (Di Giacomo *et al.*, 2018) to M_w 7.2 (Doser *et al.*, 2005), and the proposed focal depth is 15 km (ISC-GEMS catalog). The proposed focal mechanism is normal slip on a steep north–south fault, but with large uncertainties, namely, strike, dip, and rake of 207° ± 22, 54° ± 8, and −127° ± 28, respectively (Doser *et al.*, 2005).

Reid and Taber visited the area shortly after the earthquake and tsunami, and took detailed notes of the events based on interviews with eyewitnesses and inspections of the damage. Their meticulous notes and insightful interpretations published in the *Bulletin of the Seismological Society of America* in 1919 formed the basis of later modeling of the tsunami source and are summarized in Table 1. Reid and Taber (1919) observed that the wave amplitude was the highest along the northwest corner of the island, and decreased to the south and east. The wave was reported to have come from the northwest. The water along the shoreline first receded, exposing reefs that were never exposed at low tide, before returning quickly. They determined the maximum wave height from visible damage, and from eyewitness testimonies and interviewed eyewitnesses about the estimated time between the beginning of felt shaking and the initial withdrawal of the sea. The initial felt shaking was vertical, which they contrasted with the initial horizontal felt shaking during the San Francisco 1906 earthquake.

Mercado and McCann (1998) modeled the tsunami observations of Reid and Taber (1919) by assuming rupture along a fault trace marked by a dashed blue line in Figure 1. Their fault trace has a total length of 67 km, and runs along the base of the

TABLE 1
Comparison between Reid and Taber (1919) Tsunami Observations and Model Calculations

	Location of Observation	Latitude (Degree Decimal Minute)	Longitude (Degree Decimal Minute)	Observed Wave Height (m)*	Calculated Positive Amplitude (m)	Observed First Wave Polarity	Calculated First Wave Polarity	Reported Arrival Time (min) and Its Polarity†	Calculated Arrival Time (min) Matching Polarity Description
1	Pt. Agujereada	18°30.47	–67°08.24	5.5–6	6.7		N		
2	Pt. Borinquen lighthouse	18°29.32	–67°09.7	4.5	4.6	N	N		
3	Aguadilla	18°25.5	–67°09.3	2.4–3.4	2.4		N	5–6 P	6 P
4	Columbus (Colon) Park, Aguadilla	18°24.83	–67°09.73	>4	4		N		
5	Pt. Higüero lighthouse	18°21.82	–67°16.25	5.2	6	N	N		
6	Mayagüez	18°12.33	–67°09.2	1.1–1.2	1		N	25–30 P	25–32 P
7	Boquerón	18°01.56	–67°10.47	1	0.8	N	N	60 N	43–49 N
8	Rio Grande de Loíza	18°26.33	–65°52.61	1	0.7	Slight P	Slight P	25–30 N P	25–28 N P
9	Mona Island‡	18°05.28	–67°56.39	>4					

See Figure 1 for locations of observation. N, negative (withdrawal); P, positive (flooding).
*The observations did not specify the tidal condition. Tidal range around Puerto Rico is ≤0.5 m (see Data and Resources).
†Reported eyewitness arrival time and its described wave polarity (see Data and Resources for detailed description).
‡The lack of near-shore high-resolution bathymetry precludes the calculation of reliable amplitude.

entire east wall of Mona rift and crosses the rift diagonally to the southwest toward Desecheo Island at its southern end. Mercado and McCann (1998) assumed an average down-dip width of 23 km and a slip of 4 m, resulting in an earthquake magnitude of 7.47. Their model results, however, did not fit some of the documented observations. An initial positive polarity (i.e., flooding) of 0.7 m and 0.4 m was predicted in Aguadilla and Mayagüez, respectively, contrary to eyewitness reports. The maximum amplitudes were also much lower than observed. Some of the discrepancy between model predictions and the observations could probably be attributed to the coarser bathymetry available at the time (9.25 km cell size, interpolated near shore to a 90 m cell size), as well as to the lower resolution numerical model that was utilized, and the choice of fault trace location and orientation.

The discrepancy between the tsunami observations and the predictions of Mercado and McCann (1998) from a fault rupture model led López-Venegas *et al.* (2008) to explore an alternative tsunami source. High-resolution multibeam bathymetry and seismic reflection data collected since Mercado and McCann's publication revealed a 9 km × 9 km × 0.14 km landslide scar at the southern end of Mona rift (Fig. 1, inset A) with an estimated volume of evacuated material of 10 km^3 (López-Venegas *et al.*, 2008). Breaks and damage to the submarine telegraph cables, presumably due to burial by sedimentary debris, were reported within the scar area following the earthquake (Reid and Taber, 1919). The cable breaks and damage were located within the mapped landslide scar. This led López-Venegas *et al.* (2008) to propose that the tsunami was caused by an earthquake-triggered slope failure, which produced the scar (Figs. 1, 2). A similar event of earthquake-triggered landslide and turbidity currents generating a deadly tsunami was documented in Canada's Grand Banks in 1929 (Fine *et al.*, 2005 and references therein). The López-Venegas *et al.* (2008) landslide hydrodynamic model produced the initial negative polarity of the wave reaching shore, but the calculated wave amplitude was generally too high. Hornbach *et al.* (2008) reduced the volume of the modeled landslide and modified its shape to fit the observed wave amplitude. A more sophisticated modeling scheme of landslide-generated tsunami by López-Venegas *et al.* (2015) simulated the tsunami amplitude at three of the reported sites (Pt. Borinquen, Aguadilla, and Pt. Higüero; see Fig. 1 for location), but their calculated amplitudes (4.8–5.4 m, 4.8–7.2 m, and 7.1 m, respectively) did not match the Reid and Taber (1919) observed values (4.5 m, 2.4–3.4 m, and 5.2 m, respectively).

In this article, we revisit the landslide-generated tsunami hypothesis proposed by López-Venegas *et al.* (2008) using video images of the floor and walls of the landslide scar, collected by a remotely operated vehicle (ROV) and processed into a structure-from-motion 3D photogrammetric model. We also date core samples to determine the scar's age. We find that the landslide scar is older than 1918 and was likely not formed by that earthquake. We propose instead an earthquake rupture source fault that fits the negative polarity, amplitude, and arrival time of the tsunami in the reported tsunami sites, and we present seafloor images of possible fault-plane striations along the proposed source fault.

DATA

Seafloor imagery and photogrammetry

Seafloor imagery and sediment core samples within the landslide scar and along its walls were collected by the ROV Hercules

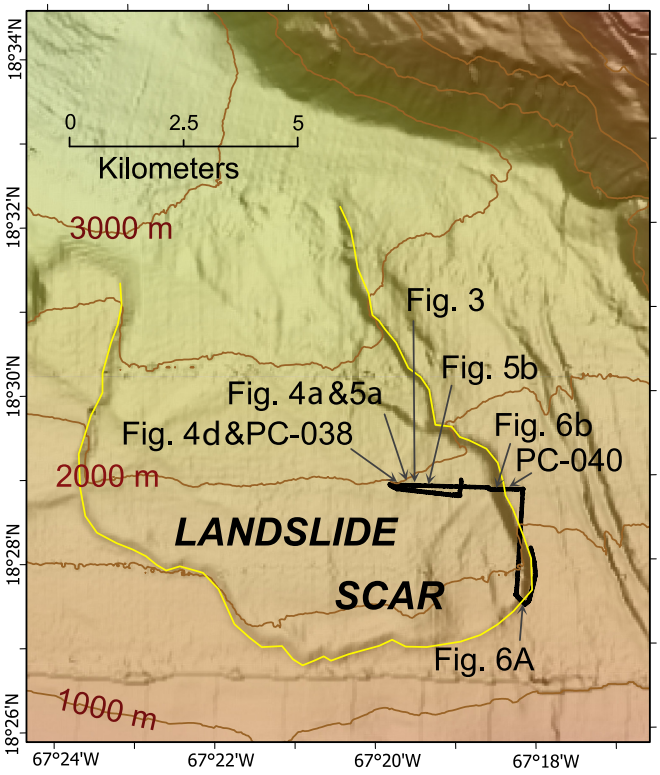

Figure 2. Enlargement of the landslide scar at the southern end of Mona rift. See Figure 1 for location. Black line denotes dive track NA035-H1301. Arrows point to site of dive images samples shown in Figures 3–6, and locations of push cores 038 and 040 discussed in Observations under the heading Sediment cores. Brown contours denote contours of water depth at 500 m interval. The color version of this figure is available only in the electronic edition.

during Dive H1301 of the Ocean Exploration Trust expedition NA-035 aboard the ship E/V Nautilus from 4 to 18 October 2013 (ten Brink *et al.*, 2014). The ROV Hercules tethered to the E/V Nautilus is equipped with a high-definition video camera, a manipulating arm for collecting rock and biological samples, push cores for collecting sediment samples, and equipment for sampling water. Hercules was illuminated by its companion ROV Argus hovering above it throughout the dives. Additional seafloor imagery of the proposed fault wall was collected during Dive 05 of the National Oceanic and Atmospheric Administration's (NOAA) Ocean Exploration Program expedition EX1502 from 9 to 30 April 2015 aboard the NOAA Ship Okeanos Explorer using its tethered ROV Deep Discoverer (Kennedy *et al.*, 2015). Throughout the dives, Deep Discoverer was illuminated by its companion ROV Seirios hovering above it.

The high-definition video collected by both Hercules and Deep Discoverer was processed into a 3D photogrammetric model. First, individual frames were extracted from the dive videos at one-second increments using Agisoft Metashape Pro. Because video images at water depths of 1000–4000 m are only illuminated by the ROV light, their color, contrast, and brightness vary between and within each frame due to the varying illumination distance and the effect of differential light attenuation by sea water. To compensate for the varying illumination distances, we balanced the brightness and contrast of the frames using OpenCV's Contrast Limited Adaptive Histogram Equalization (CLAHE) algorithm in Python. The balanced images were then imported into Agisoft Metashape Pro for processing, for which some color balance and additional brightness modification were carried out manually, in addition to masking out the edges of the ROV and deleting frames where the ROV was not moving. Although image intensity was balanced, the image color depends on the light source distance from the target rock, resulting in yellower surfaces closer to the light source and bluer surfaces farther away. From here, common processing steps were followed (e.g., Hansman and Ring, 2019) to attain a 3D photogrammetric model. The steps included aligning the images to acquire a sparse depth point cloud, refining and optimizing the camera paths using known distances and control points, building a dense point cloud from the imagery, building a 3D mesh from the dense cloud, adding navigation for georeferencing, and finally draping the imagery onto this 3D mesh and stitching 3D models into a larger matrix. These processing steps were carried out using Agisoft Metashape Pro. The 3D manipulation and display of the virtual outcrops were carried out using Virtual Outcrop Geology Group (VOG) LIME.

Hydrodynamic modeling

Tsunami simulations were carried out using the Method of Splitting Tsunamis (MOST) based on the depth-integrated nonlinear shallow water equations (Titov *et al.*, 2016). MOST simulation starts from tsunami source generation by instantaneous coseismic deformation of the seafloor. MOST then efficiently computes tsunami propagation and inundation using three nested grids to achieve increasing resolution of nearshore bathymetry and topography. Because it is the standard model used operationally at the NOAA Tsunami Warning Centers, the MOST model has been extensively verified and validated using laboratory experiments, model benchmarks, and modern tsunami events (Synolakis *et al.*, 2008; Wei *et al.*, 2008; Tang *et al.*, 2012, 2016; Wei *et al.*, 2013). Nearshore grids of one-third arcsec (~10 m) resolution were created using newer bathymetric and topographic lidar (NOAA Center of Environmental Information) collected since Andrews *et al.* (2013) database for the northeast Caribbean was published. Tsunami runup and inundation are computed. Elsewhere a reflective boundary, and thus no inundation calculation, is applied along the 1 m depth contour offshore at a grid resolution of 3 arcsec (~90 m). The MOST model uses a uniform bottom friction (Manning's) coefficient of 0.03 in all the telescoped grids.

OBSERVATIONS—LANDSLIDE SCAR IS OLDER THAN THE 1918 EARTHQUAKE

Seafloor imagery

Seismic reflection data show that the landslide scar is cut into a layered carbonate platform that had been tilted downward to

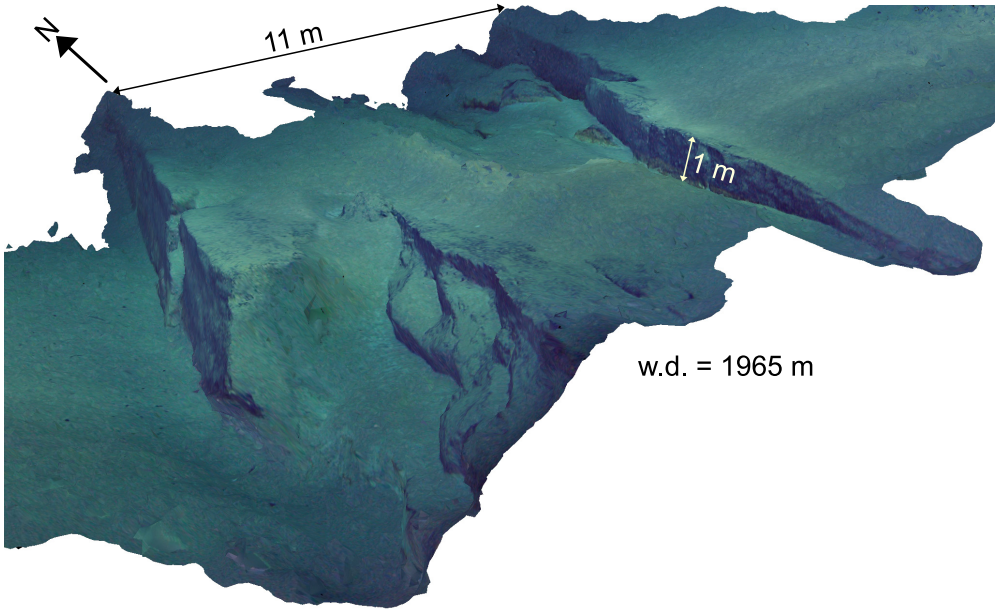

Figure 3. Image of jagged gouges in the floor of the landslide scar. Downslope direction is into the page. See Figure 2 for location. The color version of this figure is available only in the electronic edition.

the north, and both the walls and floor are made of competent limestone and dolomite (López-Venegas *et al.*, 2008). Our seafloor imagery observations show that the floor of the scar is heavily sedimented but shows evidence of jagged texture oriented in a downhill direction (e.g., Fig. 3), possibly representing frictional damage from the movements of cohesive rock against a cohesive bottom at the time of failure. The gouges are 4–8 m wide, and their edges range from a few centimeters to 1.5 m tall. The massive or layered rock faces, exposed along the edges of some gouges, are covered with black patina and show no sign of fresh breaks (e.g., Fig. 3).

The observed black patina is a Fe–Mn crust composed of Mn oxides and Fe oxyhydroxides with Mn/Fe ratios mostly around 1–2, which precipitate from seawater and envelope exposed rocks (Koschinsky and Hein, 2017; Fig. 4a,b). The patina is found throughout the world oceans. Except near hydrothermal vents, Fe–Mn crust grows at a very slow rate (1–5 mm/Ma, Maciąg *et al.*, 2019; 3.05–4.85 mm/Ma at the water depths of the dive, 1250–2000 m, Conrad *et al.*, 2017). A grab sample taken by ROV Hercules (Fig. 4c) along a deep gulley in the scar floor (see Fig. 5a for location) shows a thin (>1 mm) veneer of Fe–Mn crust on limestone. (Fig. 4b). Even a 1-μm-thick crust requires 200–1000 yr to develop. Hence, the observation of Fe–Mn crust on the gouges suggests that the gouges did not form by an earthquake-triggered landslide in 1918.

The ROV traversed a narrow gulley cut into the scar's floor (Fig. 5a). The gulley's wall is layered and most of the rock face is black, indicating the presence of Fe–Mn crust. A few rocks at the top bench of the wall appear to lack patina. The shaking from the 1918 earthquake could have dislodged a few rocks that rolled downslope. However, the gully itself does not seem to have been carved by a landslide during the 1918 earthquake. Another gully shows a white rock face at the bottom few meters of its wall (Fig. 5b). The remainder of the gully wall, however, is composed of rock ledges covered by black patina and by talus, suggesting that they were not affected by the shaking from the 1918 earthquake. Hence, it appears that some rocks may have been dislodged sporadically from a preexisting floor of the landslide scar.

The ROV traversed the eastern and southern scar walls, each >100 m high (see Fig. 6a,b for sections of these walls). The southern wall is layered, showing steep competent rock faces separated by talus and rubble (Fig. 6a). Signs of downslope sediment flow are visible, but none of them appear to be mass transport deposits from a high-volume landslide. All the exposed rock faces are black, presumably because they are covered by Fe–Mn crust (Fig. 6a). The eastern wall appears to be composed of a continuous rocky slope with pitted texture and potential layering at the base of the scarp (Fig. 6b). The primary rock texture may be hidden by the texture of the Fe–Mn crust. Fresh rock surfaces were not observed along either the eastern or southern scar walls, suggesting that the scar's walls were created before 1918. In summary, neither the floor nor the walls of the scar indicate that they formed recently; hence, we propose that the previously modeled landslide scar predates the 1918 earthquake and could not be the source of the observed tsunami.

Sediment cores

Surficial sediments recovered from ROV push cores collected within the scar (PC-038) and immediately adjacent to the crest of the eastern wall (PC-040, see Fig. 2 for location and Fig. 4d for image of the push core being pulled out of the sediment), are similar in both texture and composition. Push cores 038 and 040 penetrated 14 cm and 18 cm, respectively, but did not reach the hard-rock floor of the landslide scar. Sediment recovery was close to 100%. The sediments are composed of mixed intact and fragmented biogenic carbonate material dominated by foraminifera and pteropod tests with a small fraction of gastropod and other mollusk shells. The minor noncarbonate fraction of the sediment is composed of siliceous spicules, and detrital lithic fragments and mineral

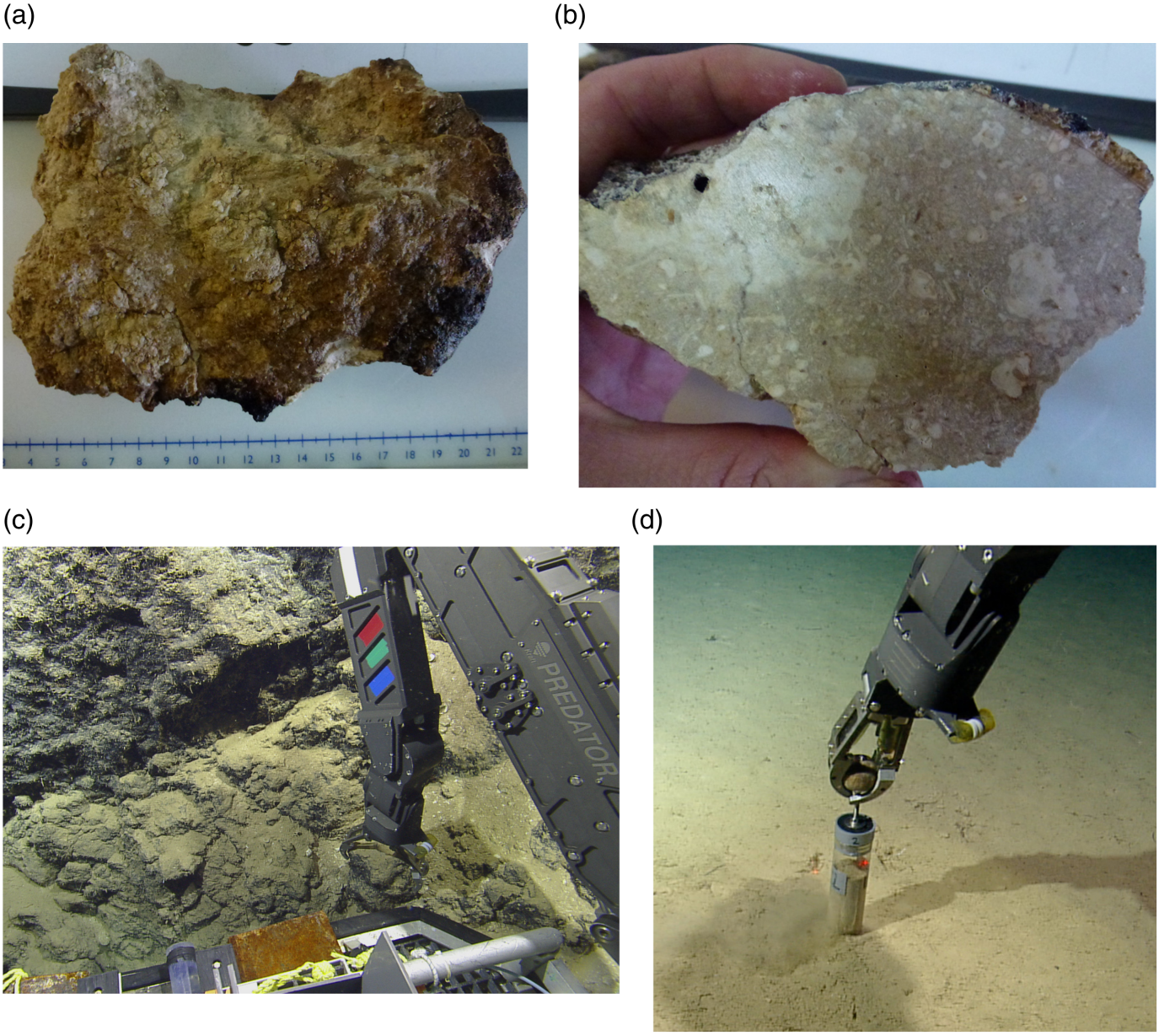

Figure 4. (a) Grab sample 2013 NA-03-039 from a gully at the scar floor at water depth of 1987 m (see Figs. 2, 5a for location) White spots are scratches caused by the ROV arm extracting the sample. (b) Sample cut in half to reveal the thickness of the Fe–Mn coating and fossiliferous biomicrite interior. (c) Photo of the ROV arm dislodging the sample from the surrounding rock. Only the rock surface exposed to seawater will show Fe–Mn coating. (d) Photo of the ROV arm extracting the push core used for sediment dating. The color version of this figure is available only in the electronic edition.

grains. The sediments are quite uniform down the cores and show no obvious signs of transport by a landslide. Texturally, the bulk of the sediments are classified as very poorly sorted (sorting > 2) clayey silts (mean grain size between 8 and 6.55φ), with minor variations in the major grain size fractions down the length of the short cores. Calcium carbonate content of the >63 μm fraction of these sediments determined by loss on ignition (Chaytor *et al.*, 2021) exceeds 60% (by weight).

Accelerator mass spectrometry ^{14}C dating was performed on planktonic foraminifera extracted from a single 1 cm thick interval in PC-038, located 3 cm below the seafloor within the scar floor at a water depth of 1973 m (see Fig. 2 for location). A calibrated age of 440 ± 120 years B.P. was determined. The calibrated age (B.P.) was calculated using Calib 8.2 (Stuiver *et al.*, 2021) and the Marine20 calibration curve (Heaton *et al.*, 2020), with only the 550 yr reservoir correction (i.e., no delta-R) applied. Based on this age, sedimentation rate appears to be relatively high on the scar's floor (6.8 cm/1000 yr). We conclude that sediment accumulation above the floor of the landslide scar likely took hundreds, if not a few thousands, years to develop.

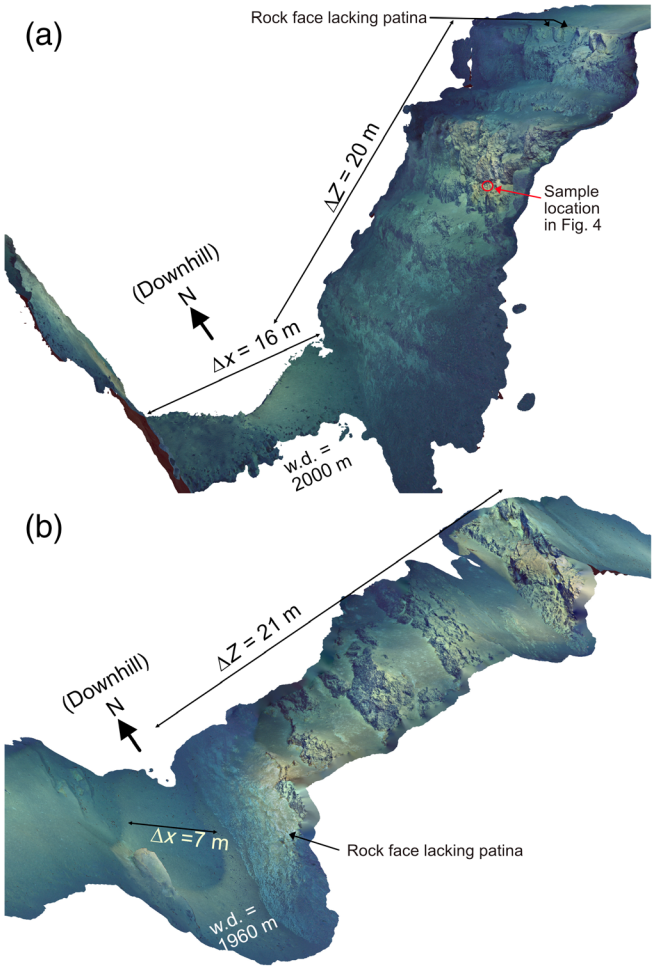

Figure 5. (a) Image of a gully cutting the floor of the landslide scar. (b) An asymmetric gully within the floor of the landslide scar. Note the white rock ledge at the base of the slope. See Figure 2 for locations of (a) and (b). Other apparent color variations in the rock face are due to variations in distance between the lighting source and the rock face. W.d., water depth. The color version of this figure is available only in the electronic edition.

DISCUSSION—SEGMENTED FAULT AS TSUNAMI SOURCE

The landslide scar in southern Mona rift likely formed several hundreds to thousands of years before 1918; hence, the tsunami could not have been generated by the associated landslide movement, as previously suggested in López-Venegas *et al.* (2008, 2015) and Hornbach *et al.* (2008). Fe–Mn crust covering both the side escarpment and gouges, and a gully on the scar's floor attest to an age of at least a few thousand years because of the slow rate of mineral precipitation from seawater onto the rock surface. A thick sediment cover of the scar's floor is dated at being older than 1918, and another obvious landslide source was not identified. Consequently, we reevaluate the possibility of a fault rupture as the source of the tsunami.

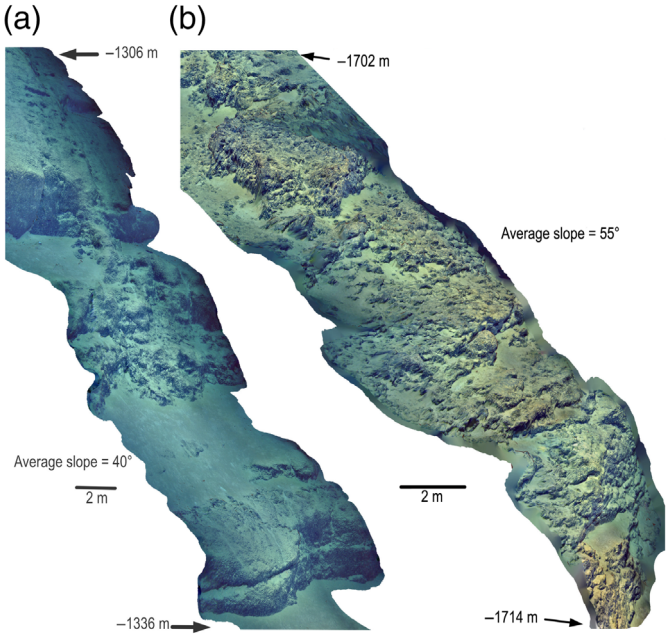

Figure 6. Images of part of (a) the southern and (b) the eastern escarpments of the landslide scar. See Figure 2 for locations of (a) and (b). The color version of this figure is available only in the electronic edition.

Tsunami models

We did not explore systematically an alternative tsunami source, but we propose here one possible source based on bathymetry, seismic profiles, dive observations, and the description of the earthquake. Our proposed fault trace is 40 km long and follows the steepest part of the bathymetric slope along the eastern and southeast walls of Mona rift (Fig. 1). Seismic reflection profiles (figs. 7 and 8 in Mondziel *et al.*, 2010; see Fig. 1 for locations) suggest a possibly active normal fault across both the orientations (Fig. 1). Dive observations discussed subsequently show a rock face with slickensides across the north–south segment. Reid and Taber (1919) described a severe shaking event followed ~2 min later by a less severe one. We propose a two-segment fault rupture scenario: a rupture of 29 km long north–south-oriented fault followed by a rupture of an 11 km long northwest–southeast-oriented fault (red rectangles in Fig. 1, Table 2). The centers of the two faults segments are ~20 km, which for an average water depth of ~3000 m will lead to positive interference between tsunami waves generated by two ruptures two minutes apart. The earthquake was initially felt as vertical motion, indicating normal faulting, which Reid and Taber (1919) contrasted with their experience during the 1906 San Francisco earthquake.

The earthquake magnitude was assumed to be M_w 7.2 following Doser *et al.* (2005). A generic dip of 60° was modeled following Doser *et al.* (2005) focal plane solution, the felt motion by eyewitnesses, and the suggested normal motion from seismic reflection data (Fig. 7; Mondziel *et al.*, 2010). A down-dip width of W = 15 km was assumed, starting 1 km below the seafloor, to

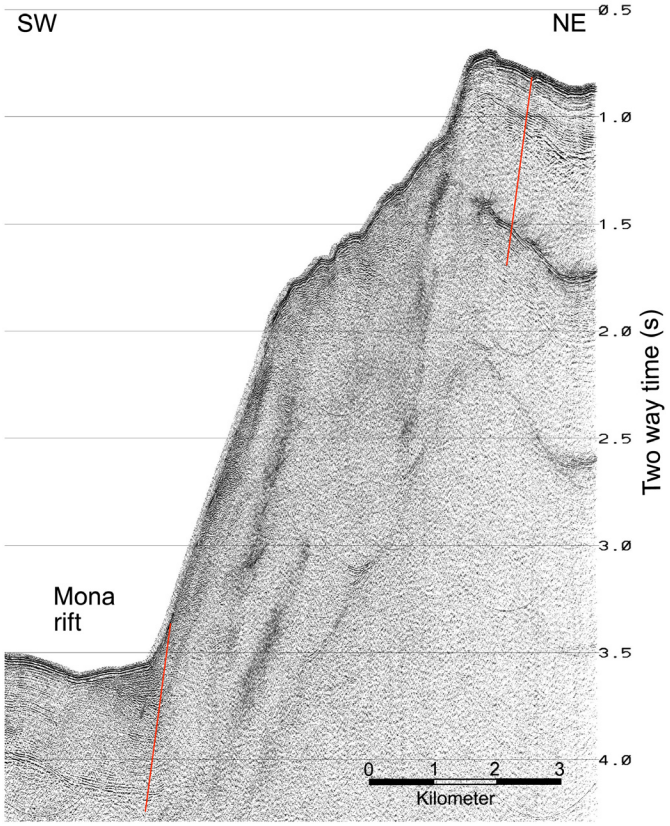

Figure 7. Portion of high-resolution multichannel seismic line 62 crossing the southeast wall of Mona rift, the possible rupture location of the 1918 earthquake and tsunami. See Figure 1 for location. Red lines denote interpreted normal fault traces. The seismic line was collected by the U.S. Geological Survey aboard the R/V Pelican. The color version of this figure is available only in the electronic edition.

avoid a singularity in the calculation (Fig. 8). The modeled fault parameters are listed in Table 2.

The calculated tsunami amplitude, polarity, and arrival time from this rupture source fit reported observations of Reid and Taber (1919) (Table 1, Fig. 9). The misfits in wave amplitude are <1 m. The observations of Reid and Taber (1919) did not specify the tidal level during the tsunami, which around Puerto Rico is ≤0.5 m (see Data and Resources). Reid and Taber (1919) did not specify the tsunami observation location along the Aguadilla shoreline. However, LaForge and McCann (2017) and López-Venegas *et al.* (2015) used archival petitions for funds to repair tsunami damage to identify the exact street in Aguadilla, which suffered the maximum damage. The shoreline coordinate facing that street was used in Table 1. A map of the maximum predicted flooding from the two-segment fault rupture is shown in Figure 10.

The modeled first wave polarity at all reported sites fits the eyewitness reports. Reid and Taber (1919) reported initial withdrawal in all locations except in Loíza (Fig. 9). Except for Boquerón, the calculated arrival time fit the eyewitness reports in Reid and Taber (1919). Flooding at 5–6 min and 25–30 min after the shaking was felt was reported in Aguadilla and Mayagüez, respectively. A withdrawal followed by flooding 25–30 min after the earthquake was reported in Loíza, and withdrawal about 1 hr after the earthquake was reported in Boquerón.

Fault-plane imagery

Exposed fault planes may have been encountered on a dive across the fault trace proposed by our tsunami model. Video observations collected by ROV Deep Discoverer along the east wall of Mona rift between depths of 3300 and 4000 m, encountered Late Cretaceous to Middle Eocene meta-volcanic and plutonic rocks that form the core of Puerto Rico Island underlying the Late Oligocene to Pliocene platform carbonate sequence. Slickensides (smooth, striated, and corrugated surface) were identified at depths of 3884–3882 m (Figs. 1a, 11a). Slickensides are thought to be produced by frictional rock movement along a fault. The rock surface of the slickensides is free of Fe–Mn crust, indicating that this rock face is likely recently exposed. The striations point downward, indicating subvertical movement. Their slope, 20 ± 8°, is lower than the 60° slope assumed in our tsunami model, and their dip direction is 190° ± 10°, suggesting that the striations have developed along a subsidiary fault plane. A smooth rock face lacking patina is also observed a few meters above the striations (Figs. 1a, 11b). A bluish color exposure at the bottom of the image with possible striations may be a small fault-plane exposure and/or a freshly exposed blueschist (enlargement in

TABLE 2
Fault Rupture Parameters for the Tsunami Model

Segment	Length (km)	Down-Dip Width (km)*	Slip (m)	Latitude (Degree Decimal Minute)	Longitude (Degree Decimal Minute)	Latitude (Degree Decimal Minute)	Longitude (Degree Decimal Minute)	Strike (°)	Dip (°)	Rake (°)
1	29	15	4.32	18°51.67	–67°18.14	18°36.18	–67°20.98	190	60	–90
2	11	15	4.32	18°34.09	–67°18.65	18°32.18	–67°13.50	109	60	–90

*Fault top is at 1 km depth. Shear modulus μ=3×10^{10} Pa.

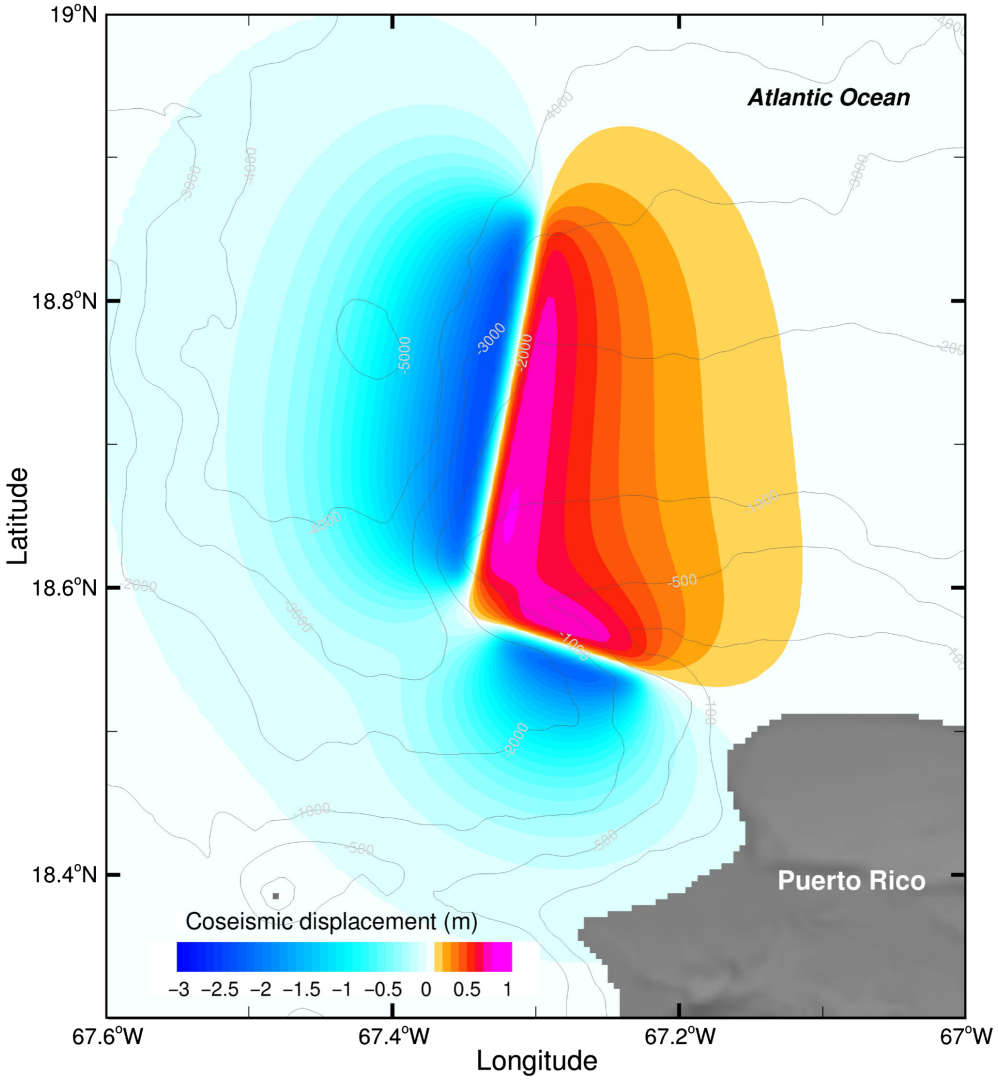

Figure 8. Initial sea surface and sea floor displacement in the tsunami model due to the rupture of a two-segmented normal fault discussed in Discussion—segmented fault as tsunami source section. Contours are simplified bathymetry (in meters). The color version of this figure is available only in the electronic edition.

Fig. 11b). The dip direction of this exposure is 280°. A late Cretaceous blueschist belt extending along the continental slope eastward from Samaná Peninsula in the northeast Dominican Republic was proposed by Perfit *et al.* (1980) from analysis of outcrops and dredges.

CONCLUSIONS

The source of the devastating 1918 western Puerto Rico tsunami had previously been ascribed to both an earthquake fault rupture (Mercado and McCann, 1998) and an earthquake-triggered landslide (Hornbach *et al.*, 2008; López-Venegas *et al.*, 2008, 2015). Documented landslide tsunami sources are rare, and the landslide source for the 1918 tsunami had been cited as an example for landslide tsunami hazards (e.g., National Research Council, 2011). The landslide source suggestion was based on the then newly available ship-board high-resolution multibeam bathymetry and seismic reflection data, coupled with reports about submarine cable breaks within the landslide scar area (Reid and Taber, 1919). An in situ examination of the floor and walls of the landslide scar, using high-definition video from an ROV, and core samples collected by the ROV suggest, however, that the scar is at least several hundred years old and, therefore, the landslide that formed could not have been triggered by the 1918 earthquake. The evidence includes a relatively thick sediment cover of the hard carbonate scar floor, dated at several hundred years old or more, and the observations of extensive Fe–Mn crust of the exposed rock faces of the eastern and southern escarpment, the gouges in the scar floor, and in gullies cut into the scar floor. Published estimates of Fe–Mn crust precipitation from seawater in the absence of hydrothermal activity is 1–5 mm/Ma. The reported submarine cable damage and breaks could be caused by smaller rock falls from steep outcrops, and not by the presumed movement of a 140 m thick, 9 km wide tsunami-generating landslide.

We propose an alternative tsunami source, namely, a two-segmented normal-fault rupture along the steepest parts of the eastern wall of Mona rift northwest of Puerto Rico. Our proposed fault rupture has a total magnitude of M_w 7.2 and parameters that are compatible with seismic reflection observations and with seismic analysis of the historical seismograms (Doser *et al.*, 2005; Di Giacomo *et al.*, 2018). Although we have not performed a rigorous search for the best tsunami source location and parameters, our hydrodynamic model simulates with fidelity the amplitudes, the first wave polarities, and the arrival times at eight sites along western and northern Puerto Rico, which were reported by Reid and Taber (1919). An ROV dive along the proposed ruptured fault reveals possible

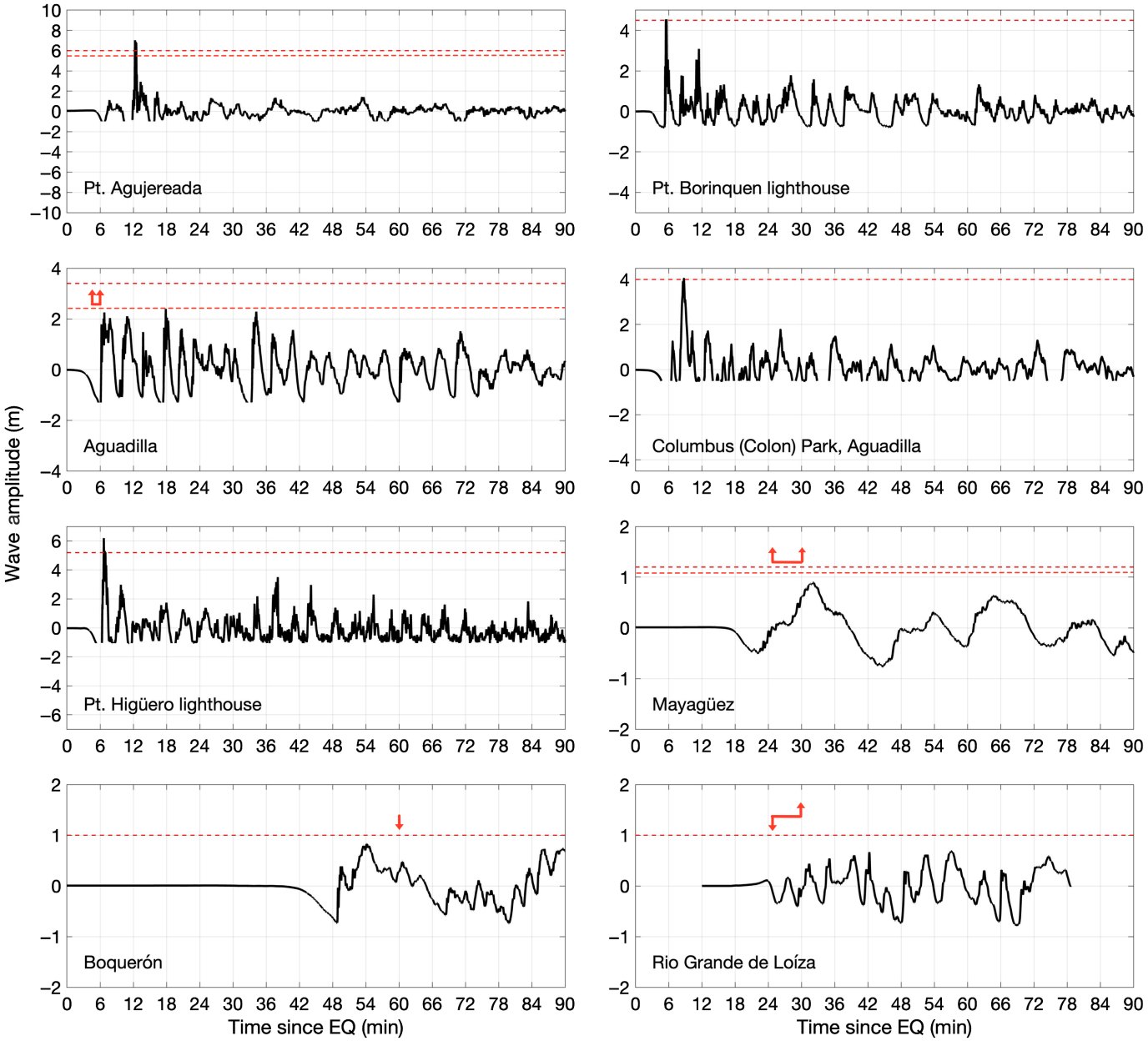

corrugated striations in the exposed hard rock (slickensides) that can be interpreted as being formed by friction along a fault plane. Some of the hard-rock face in the surrounding area is devoid of Fe–Mn crust. Our analysis, thus, demonstrates the importance of in situ observations and sampling for natural hazard studies in the ocean.

Figure 9. Calculated marigrams at the observation sites listed in Table 1. Observation sites are shown in Figure 1. Missing negative parts of the marigrams at several sites occur when the seafloor gets exposed (dry) during water withdrawal, because calculated sites are located at water depths between 0.5 and 2 m. Red dashed line denotes the maximum observed tsunami height from Reid and Taber (1919). Two lines are marked where a range of heights was quoted. Red arrows denote observed arrival time of the tsunami wave, described in Reid and Taber (1919) and listed in Data and Resources. The arrow directions describe rising water (up arrow) or receding water (down arrow). Arrows are separated by a horizontal line that denotes range of arrival time. The color version of this figure is available only in the electronic edition.

DATA AND RESOURCES

Videos collected during the National Oceanic and Atmospheric Administration's (NOAA) Ocean Exploration cruise EX1502 are available from NOAA's video archive portal https://www.ncei.noaa.gov/access/ocean-exploration/video/ (last accessed March 2020). Core samples are available at https://web.uri.edu/gso/research/marine-geological-samples-laboratory/ (last accessed March 2020). Ocean Exploration Trust videos from expedition NA-035 are available upon request at https://nautiluslive.org/science/data-management (last accessed March 2020). Seismic parameters of the 1918 earthquake were retrieved from the International Seismological Center–Global Earthquake Model (ISC-GEMS) catalog at doi: 10.31905/D808B825 (last accessed June 2022). OpenCV's (https://opencv.org, last accessed March 2020) Contrast

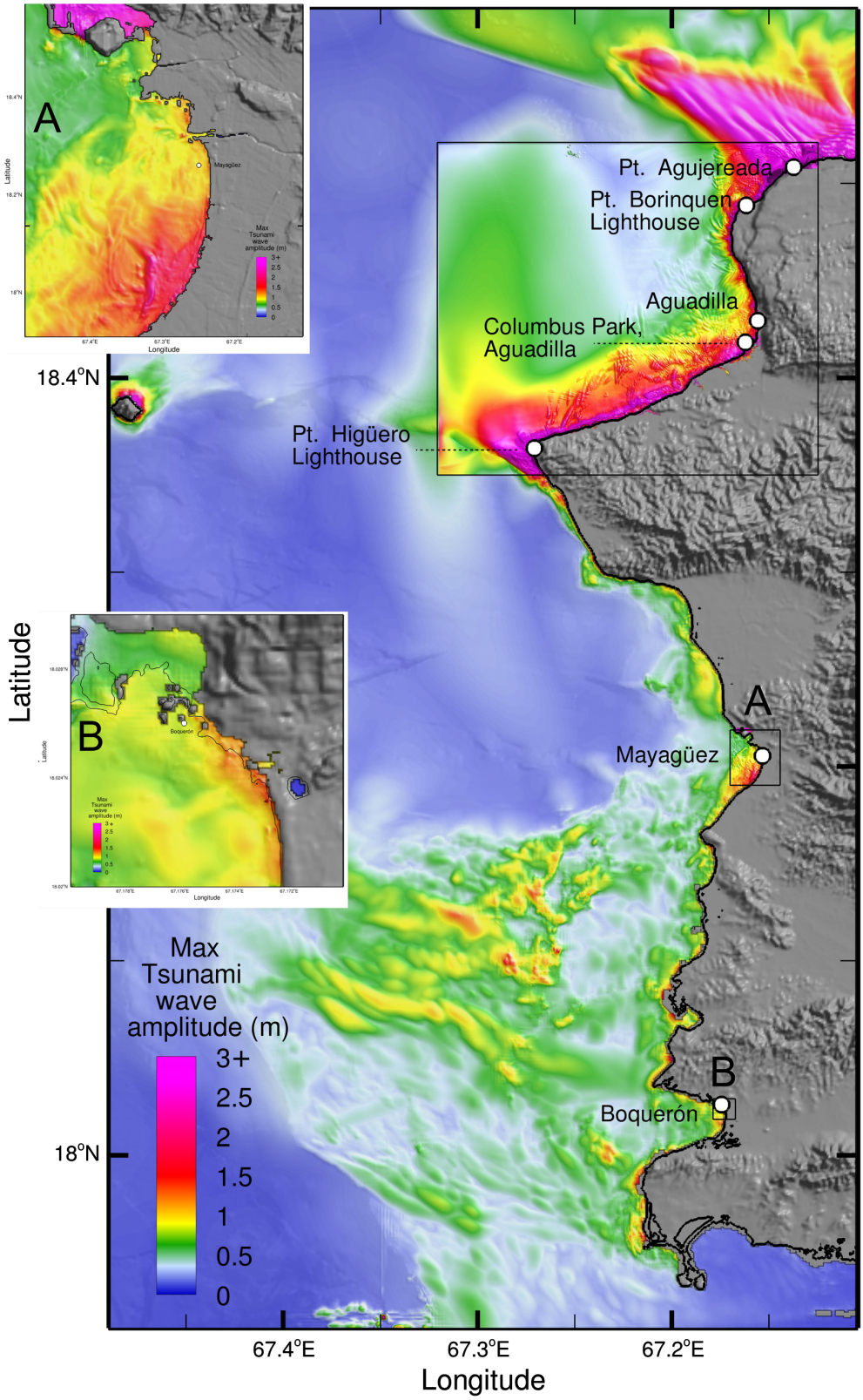

Figure 10. Calculated maximum tsunami wave amplitude along the west coast of Puerto Rico due to the two-segmented normal fault along the east wall of Mona rift. Rectangles denote areas modeled using 10 m grid spacing. White circles denote locations of tsunami observations in Reid and Taber (1919). Insets A and B shows the enlargements of the rectangles near Mayagüez and Boquerón. The color version of this figure is available only in the electronic edition.

Limited Adaptive Histogram Equalization (CLAHE) algorithm can be downloaded from the openCV package https://opencv.org/releases/ (last accessed September 2022). The seismic profile in Figure 7 is available at https://walrus.wr.usgs.gov/namss/survey/p-30-06-cb/ (last accessed September 2022). The information about NOAA tides and current is available at https://tidesandcurrents.noaa.gov/ (last accessed November 2022). Following is the description of the observed tsunami arrival times and their polarities in Reid and Taber (1919): Aguadilla: "Estimates of the time interval between the earthquake shock and the arrival of the sea wave, made by different observers, range from four to seven minutes, one of the best being five to six minutes" (p. 110). Mayagüez: "In the interval between the earthquake and the arrival of the sea wave, an automobile traveled from the Central Corsica near Rincon to Mayagüez, a trip that is estimated to require twenty-five or thirty minutes" (p. 112). El Boqueron: "An observer states that the ocean withdrew about an hour after the earthquake, the water going out gradually during a period of twenty minutes" (p. 112). Loíza:".reported to have subsided and then to have risen about one meter above normal, the phenomenon occurring twenty-five or thirty minutes after the earthquake" (p. 113).

DECLARATION OF COMPETING INTERESTS

The authors acknowledge that there are no conflicts of interest recorded.

ACKNOWLEDGMENTS

The authors are indebted to Robert Ballard and Ocean Exploration Trust, and to National Oceanic and Atmospheric Administration's (NOAA) Ocean Exploration Program for the use of their ships, remotely operated vehicles (ROVs),

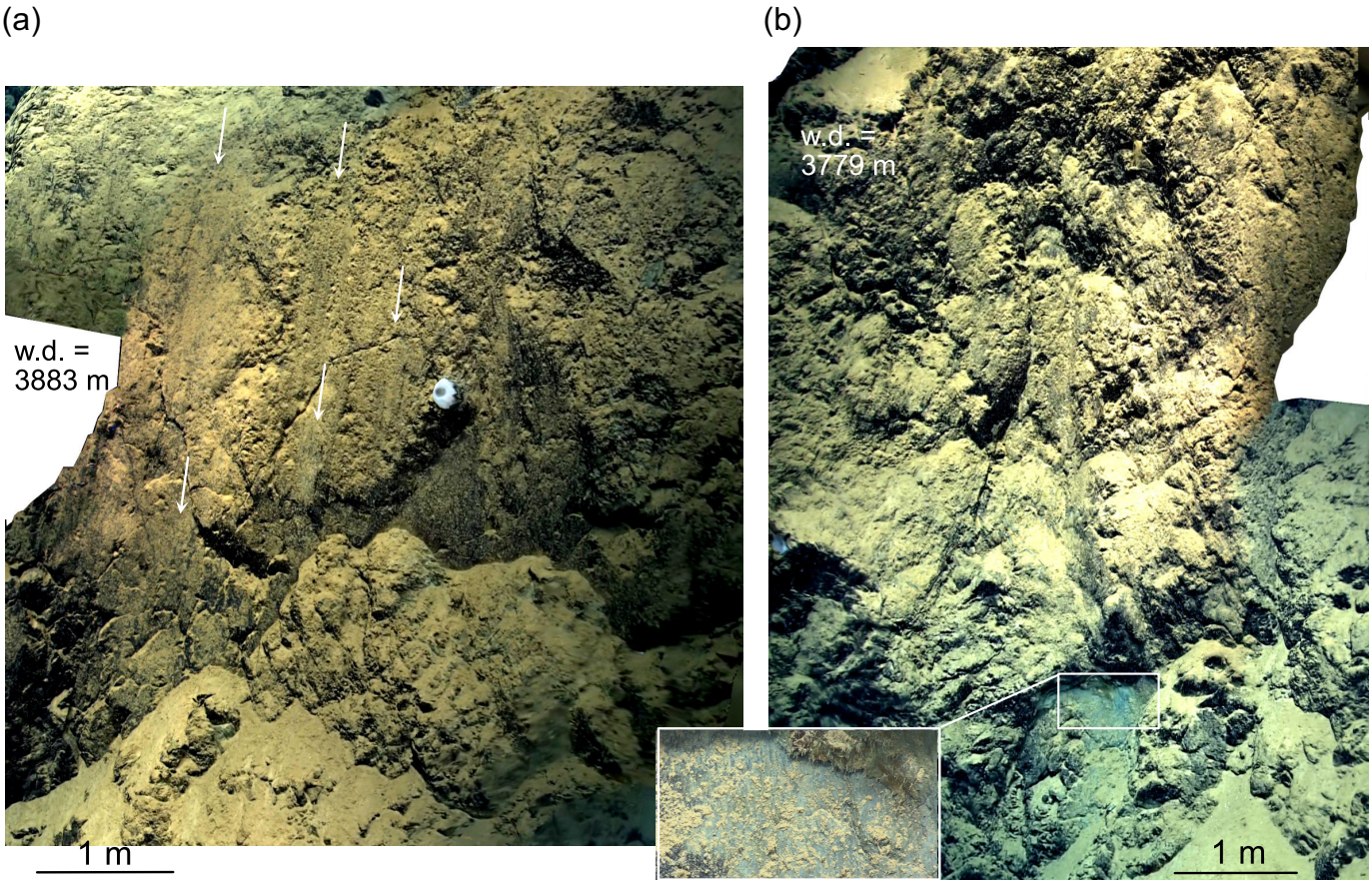

Figure 11. (a) Slickensides (pointed by white arrows) on plutonic (likely plutonic) rock. See inset B in Figure 1 for location. "White flower"—Sponge (b) massive plutonic (likely plutonic) rock without Fe–Mn crust. Enlargement —A small blueish smooth surface, possibly, an exposed fault plane in direction 280°. The rock may be a blueschist outcrop. The color version of this figure is available only in the electronic edition.

and technical expertise. The authors thank Dwight Coleman, Amanda Demopoulos, Nicole Reineault, Brian Kennedy, Mike Cheadle, Andrea Quattrini, and the rest of the onboard and remote participants in cruises NA-035 and EX1502. Bill Danforth helped with the initial processing steps. Helpful reviews by Wayne Baldwin, Matias Carvajal, and Alberto López-Venegas are gratefully acknowledged. Yong Wei's work is funded by the Cooperative Institute for Climate, Ocean, & Ecosystem Studies (CIOCES) under NOAA Cooperative Agreement NA20OAR4320271, Contribution Number 2022-1234, PMEL Contribution Number 5401. Simon Detmer's and Lilian Lucas's work was funded by the Woods Hole Oceanographic Institution Summer Student Fellowship. Aggeliki Georgiopoulou thanks the Fulbright Foundation and Geological Survey Ireland for enabling her research stay at U.S. Geological Survey (USGS) Woods Hole Coastal and Marine Science Center.

Any use of trade, firm, or product names is for descriptive purposes only and does not imply endorsement by the U.S. Government.

REFERENCES

Andrews, B. D., U. S. ten Brink, W. W. Danforth, J. D. Chaytor, J.-L. Granja-Bruna, P. Llanes Estrada, and A. Carbo-Gorosobel (2013). Bathymetric terrain model of the Puerto Rico Trench and Northeast Caribbean for marine geological investigations, *U.S. Geol. Surv. Open File Rept. 2013-1125*, 10 pp, doi: 10.3133/ofr20131125.

Chaytor, J. D., and U. S. ten Brink (2010) Extension in Mona Passage, Northeast Caribbean, *Tectonophysics* **493,** 74–92.

Chaytor, J. D., M. S. Ballard, B. J. Buczkowski, J. A. Goff, K. M. Lee, A. H. Reed, and A. A. Boggess (2021). Measurements of geologic characteristics and geophysical properties of sediments from the New England Mud Patch, *IEEE J. Ocean. Eng.* **99,** 1–28.

Conrad, T., J. R. Hein, A. Paytan, and D. A. Clague (2017). Formation of Fe-Mn crusts within a continental margin environment, *Ore Geol. Rev.* **87,** 25–40.

Di Giacomo, D., E. R. Engdahl, and D. A. Storchak (2018). The ISC-GEM earthquake catalogue (1904–2014): Status after the Extension Project, *Earth Syst. Sci. Data* **10,** 1877–1899, doi: 10.5194/essd-10-1877-2018.

Doser, D., C. Rodríguez, C. Flores, and P. Mann (2005). Historical earthquakes of the Puerto Rico-Virgin Island region, in *Active Tectonic and Seismic Hazards of Puerto Rico, the Virgin Islands, and Offshore Areas*, P. Mann (Editors), Geological Society of America, Boulder, Colorado, 103–114.

Fine, I. V., A. B. Rabinovich, B. D. Bornhold, R. E. Thomson, and E. A. Kulikov (2005). The Grand Banks landslide-generated tsunami of November 18, 1929: Preliminary analysis and numerical modeling, *Mar. Geol.* **215,** 45–57.

Hansman, R. J., and U. Ring (2019). Workflow: From photo-based 3-D reconstruction of remotely piloted aircraft images to a 3-D geological model, *Geosphere* **15,** 1393–1408.

Heaton, T. J., P. Köhler, M. Butzin, E. Bard, R. W. Reimer, W. E. Austin, C. B. Ramsey, P. M. Grootes, K. A. Hughen, B. Kromer, *et al.* (2020). Marine20—The marine radiocarbon age calibration curve (0–55,000 cal BP), *Radiocarbon* **62,** 779–820.

Hornbach, M. J., S. A. Mondziel, N. R. Grindlay, C. Frohlich, and P. Mann (2008). Did a submarine slide trigger the 1918 Puerto Rico tsunami? *Sci. Tsunami Haz.* **27,** 22–31.

Kennedy, B. R. C., K. Cantwell, D. Sowers, A. M. Quattrini, M. J. Cheadle, and L. McKenna(2015). EX1502L3 Expedition Report-Oceana Profundo 2015: Exploring Puerto Rico's Seamounts, Trenches, and Troughs, *Office of Ocean Exploration and Research, Office of Oceanic &Atmospheric Research, NOAA, Silver Spring, MD 20910. OER Expedition Rep. 2015-02-03*, 93 pp, doi: 10.7289/V5NG4NM8.

Koschinsky, A., and J. R. Hein (2017). Marine ferromanganese encrustations: Archives of changing oceans, *Elements* **13,** 177–182.

LaForge, R., and W. R. McCann (2017). Address-level effects in Aguadilla, Puerto Rico, from the 1918 Mw 7.3 earthquake and Tsunami, *Seismol. Res. Lett.* **88,** 1316–1321.

López-Venegas, A. M., J. Horrillo, A. Pampell-Manis, V. Huérfano, and A. Mercado (2015). Advanced tsunami numerical simulations and energy considerations by use of 3D–2D coupled models: The October 11, 1918, Mona passage tsunami, *Pure Appl. Geophys.* **172,** 1679–1698.

López-Venegas, A. M., U. S. ten Brink, and E. L. Geist (2008). Submarine landslide as the source for the October 11, 1918 Mona Passage tsunami: Observations and modeling, *Mar. Geol.* **254,** 35–46.

Maciąg, Ł., D. Zawadzki, G. A. Kozub-Budzyń, A. Piestrzyński, R. A. Kotliński, and R. J. Wróbel (2019). Mineralogy of cobalt-rich ferromanganese crusts from the Perth Abyssal Plain (E Indian Ocean), *Minerals* **9,** 84.

Mercado, A., and W. R. McCann (1998). Numerical simulation of the 1918 Puerto Rico Tsunami, *Nat. Hazards* **18,** 57–76.

Mondziel, S., N. Grindlay, P. Mann, A. Escalona, and L. Abrams (2010). Morphology, structure, and tectonic evolution of the Mona canyon (northern Mona passage) from multibeam bathymetry, side-scan sonar, and seismic reflection profiles, *Tectonics* **29,** doi: 10.1029/2008TC002441.

National Research Council (2011). *Tsunami Warning and Preparedness: An Assessment of the U.S. Tsunami Program and the Nation's Preparedness Efforts*, The National Academies Press, Washington, D.C.

Perfit, M. R., B. C. Heezen, M. Rawson, and T. W. Donnelly (1980). Chemistry, origin and tectonic significance of metamorphic rocks from the Puerto Rico Trench, *Mar. Geol.* **34,** 125–156.

Reid, H. F., and S. Taber (1919). The Porto Rico earthquakes of October-November, 1918, *Bull. Seismol. Soc. Am.* **9,** 95–127.

Russo, R. M., and C. Bareford (1993). Historical seismicity of the Caribbean region, 1933–1963, *Caribbean Conf. on Volcanism, Seismicity and Earthquake Engineering*, University of the West Indies, Trinidad, October 1993.

Stuiver, M., P. J. Reimer, and R. Reimer (2021). CALIB radiocarbon calibration 8.2, available at http://calib.org/calib/calib.html (last accessed March 2021).

Synolakis, C. E., E. N. Bernard, V. V. Titov, U. Kanoglu, and F. I. Gonzalez (2008). Validation and verification of tsunami numerical models, *Pure Appl. Geophys.* **165,** 2197–2228.

Tang, L., V. V. Titov, E. N. Bernard, Y. Wei, C. Chamberlin, J. C. Newman, H. Mofjeld, D. Arcas, M. Eble, C. Moore, *et al.* (2012). Direct energy estimation of the 2011 Japan tsunami using deep-ocean pressure measurements, *J. Geophys. Res.* **117,** no. C8, doi: 10.1029/2011JC007635.

Tang, L., V. V. Titov, C. Moore, and Y. Wei (2016). Real-time assessment of the 16 September 2015 Chile Tsunami and implications for near-field forecast, *Pure Appl. Geophys.* **173,** 369–387, doi: 10.1007/s00024-015-1226-3.

ten Brink, U., D. F. Coleman, J. Chaytor, A. W. J. Demopoulos, R. Armstrong, G. Garcia-Moliner, N. A. Raineault, B. Andrews, R. Chastain, *et al.* (2014). Earthquake, landslide, and Tsunami hazards and benthic biology in the Greater Antilles, *Oceanography* **27,** 34–35.

Titov, V. V., U. Kânoğlu, and C. Synolakis (2016). Development of MOST for real-time tsunami forecasting, *J. Waterw. Port Coast. Ocean Eng.* **142,** 03116004, doi: 10.1061/(ASCE)WW.1943-5460.0000357.

Wei, Y., E. N. Bernard, L. Tang, R. Weiss, V. V. Titov, C. Moore, M. Spillane, M. Hopkins, and U. Kânoğlu (2008). Real-time experimental forecast of the Peruvian Tsunami of August 2007 for U.S. coastlines, *Geophys. Res. Lett.* **35,** L04609 , doi: 10.1029/2007GL032250.

Wei, Y., C. Chamberlin, V. V. Titov, L. Tang, and E. N. Bernard (2013). Modeling of the 2011 Japan Tsunami—Lessons for near-field forecast, *Pure Appl. Geophys.* **170,** 1309–1331, doi: 10.1007/s00024-012-0519-z.

Manuscript received 18 July 2022
Published online 3 January 2023